Materials Horizons

Controlling nano- and microfilament morphology by strategically placing chiral centers in the side chains of bent-core molecules

Journal:	*Materials Horizons*
Manuscript ID	MH-COM-09-2024-001243.R1
Article Type:	Communication
Date Submitted by the Author:	01-Oct-2024
Complete List of Authors:	Gowda Muniyappa, Ashwathanarayana; Kent State University, Advanced Materials and Liquid Crystal Institute Acherjee, Gourab; Kent State University, Department of Chemistry and Biochemistry and Advanced Materials and Liquid Crystal Institute Pathak, Suraj; Kent State University, Advanced Materials & Liquid Crystal Institute Rohaley, Grace; Kent State University, Materials Science Graduate Program, Advanced Materials and Liquid Crystal Institute Shah, Asmita; Kent State University, Advanced Materials & Liquid Crystal Institute Lemieux, Robert; University of Waterloo, Chemistry Prévôt, Marianne; Kent State University, AMLCI Hegmann, Torsten; Kent State University, Liquid Crystals

New concepts statement

We demonstrate that the shape or morphology of self-assembled organic nano- and microfilaments can be preconceived by logical molecular design. For a series of molecules with a pronounced bent molecular shape, these design concepts rely on a priori molecular conformational analysis coupled with the rational placement of chiral centers at the junctions between the rigid aromatic cores and the flexible aliphatic side chains. The complete series now illuminates the full morphological transition from flat microribbons to strongly twisted helical nanofilaments. In due course, we discovered complex new morphologies including, for example, flat multilayer microribbons that gradually decrease in width—in analogy to down feathers or split hair ends—to ultimately twist at the ends as well as nanofilaments that untwist at their ends or mid filament, notably without any perversions. Altogether, combined with existing morphologies formed by tris-biphenyl bent-core molecules, these new morphologies serve as snapshots to illuminate the entire possible transformation, from flat multilayer ribbons over writhed nanocylinders and microfilaments mimicking bladed worm corkscrews to helical nanofilaments with negative Gaussian curvature. Relevant for numerous applications, these nano- and microfilaments can serve as templates for nanomaterials or emitters, among other materials, and display structural coloration that varies with the dimensions of the ultimate filament.

COMMUNICATION

Controlling nano- and microfilament morphology by strategically placing chiral centers in the side chains of bent-core molecules†

Received 00th August 2024,
Accepted 00th January 2024

DOI: 10.1039/x0xx00000x

Ashwathanarayana Gowda,[a] Gourab Acharjee,[b] Suraj Kumar Pathak,[a] Grace A.R. Rohaley,[ac] Asmita Shah,[a] Robert P. Lemieux,[d] Marianne E. Prévôt*[a-c] and Torsten Hegmann*[abce]

Self-assembled lamellar nano- and microfilaments formed by select types of bent-core molecules are prime examples of the interplay between molecular conformation and morphological chirality. Here, we demonstrate how the strategic placement of chiral centers at C-1 and/or C-3 in the terminal alkyloxy side chains, largely based on a priori calculations of molecular conformation, leads to the predictable formation of increasingly complex nano- and microfilament morphologies. Adding to the previosuly described diversity of twisted and writhed filament types, we here demonstarte and explain the formation and coexistence of flat nanoribbons, nanocylinders, or nano- as well as microfilaments where the morphology spontaneously changes along the filament long axis. For some these more exotic types of filament morphology, helical multilayer filaments suddenly unwind to form flat nanoribbons that also twist again under preservation (not perversion) of the helical twist sense. Moreover, the morphologies formed by this series of molecules now allows us to demonstrate the complete transformation from flat multilayer ribbons over microfilaments and helical-wrapped nanocylinders to helical nanofilaments depending on the number and position of chiral centers in the aliphatic side chains.

1. Introduction

Chiral filament morphologies are omnipresent building blocks in nature, found equally in flora and fauna at length scales ranging in length or width from a few nanometers to multi-meter-long macroscopic objects.[1-9] In materials science, chiral filaments with nano- or microscale dimensions are increasingly generated using a wide array of materials classes and studied for promising uses in optics, photonics, sensing, and many other purposes.[10]

The most common filament morphologies comprise single rod- or flat ribbon subfilaments or several individual subfilaments stacked on top of or twisting around one another with the cross-sections of the final multi-layer filaments being flat, elliptical, or round.[10]

The flat (lamellar) ribbons, as basic building blocks for the family of B4 filaments formed by molecules with a pronounced bent molecular shape, have been shown to assemble into multilayer helicoids, helical ribbons (cylindrical helices), or flat as well as occasionally twisted nanoribbons depending on the number and position of chiral centers in either one or both aliphatic side chains.[11] Here, continuous twisting along a straight centerline leads to twisted multilayer filaments with Gaussian saddle-like curvature, continuous bending around the width of the ribbons to cylindrical helices with a helical centerline.[10]

The original helical nanofilament or HNF phase, appropriately named after the discovery of its internal structure and overall morphology by Clark *et al.*, is a perfect example of self-assembly directed by molecular conformation.[12] Multilayer helicoids form due to an intralayer mismatch between the two molecular halves that can only be relieved by local saddle splay. This, in turn, leads to twisted filaments composed of a limited number of layer stacks (about 5−7 layers). An intralayer mismatch is here the inherent misfit (in an anisotropic multi-layer configuration) that leads to twist.[13] The two molecular halves tilt in orthogonal directions from the layer mid-plane (i.e., each at a subfilament angle of $\theta \sim 45°$) that generates a continuous twist of the flat ribbon along a straight center- line of about 2° nm^{-1} forming a helicoid. When formed by achiral molecules, HNFs exist as a chiral conglomerate composed of macroscopic chiral domains with opposite handedness.[12] Within each domain, HNFs grow, chirality preserving (left-handed in one domain and right-handed in an adjacent domain),[14] with a preset bulk secondary twist among HNFs governed by excluded volume interactions of strongly twisted filaments (i.e., right-handed HNFs form a right-handed secondary twist and vice versa).[15-17] Early portrayal of this phase, historically named the B4 phase, was that of a crystalline solid phase.[18] However, solid-state magic-angle spinning (MAS)-NMR experiments clarified that the HNF phase is neither a traditional crystalline solid nor a conventional liquid crystal[19] that is also characterized by crystal or hexatic in-layer ordering.[12]

Morphological variants of the classical HNFs now include helical nano- and microfilaments with varying dimensions[20-24] (width,

[a] Advanced Materials and Liquid Crystal Institute, Kent State University, Kent, OH 44242, USA. E-mail: thegmann@kent.edu; mprevot1@kent.edu
[b] Department of Chemistry and Biochemistry, Kent State University, Kent, OH 44242, USA
[c] Materials Science Graduate Program, Kent State University, Kent, OH 44242, USA
[d] Department of Chemistry, University of Waterloo, Waterloo, Ontario N2L 3G1, Canada
[e] Brain Health Research Institute, Kent State University, Kent, OH 44242, USA

† Electronic Supplementary Information (ESI) available: Synthesis details; analytical data; DSC data; additional SEM and TEM images. See DOI: 10.1039/x0xx00000x

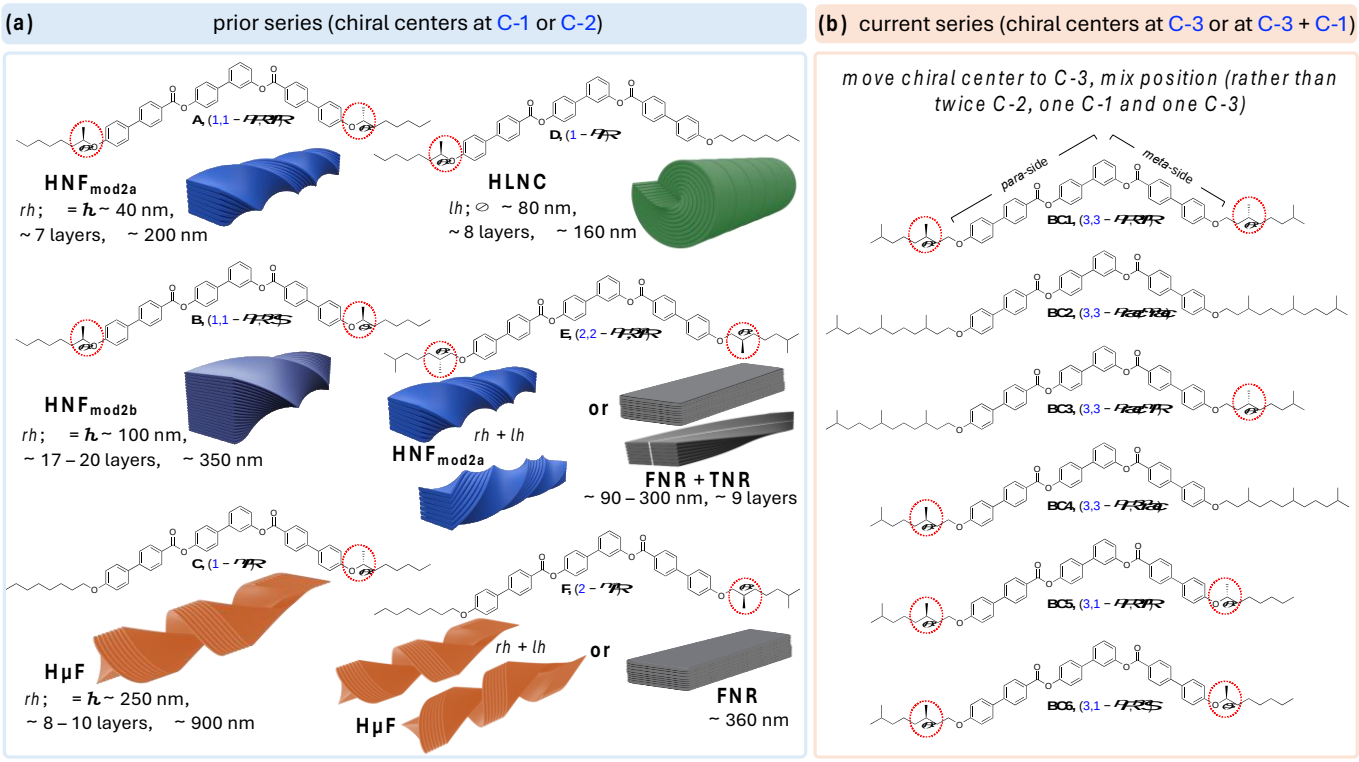

Figure 1. (a) Structures of tris-biphenyl bent-core molecules **A** – **F**[20-22, 28] with chiral centers at C-1 or C-2 in the aliphatic side chains and type (incl. handedness, dimensions, and number of layers) of nano- or microfilament formed depending on the rate of cooling from the isotropic liquid (*rh* = right-handed, *lh* = left-handed, *w* = width, *ħ* = height, *p* = pitch, and ∅ = diameter). (b) Chemical structures of the new series with chiral centers at C-3 (**BC1** – **BC4**) or at C-1 in the shorter *meta*-side and C-3 in the longer *para*-side (**BC5** and **BC6**).

height, and helical pitch) and intra- or interlayer modulation (**A**-**C**, Figure 1a), heliconical nanocrystallites,[25] heliconical-layered nanocylinders[26, 27] (**D**, Figure 1a), and flat or occasionally twisted flat nanoribbons[28] (**E** and **F**, Figure 1a). The majority of these flat, twisted, or cylindrical nano- or microfilament morphologies were realized by strategically incorporating chiral centers into the aliphatic side chains of tris-biphenyl aromatic core bent-core molecules.[10, 11] Noteworthy, all these morphologies display characteristic blue structural color in reflection mode, whose origin is not fully understood but surely linked to diffraction, scattering, or interference via the periodic nano- to microscale layering and packing of these filaments in thin films.[29-31]

Single-molecule stochastic dynamics (SD) atomistic simulations as well as density functional theory (DFT) calculations (B3LYP/6-31G*) revealed that the position of the chiral center at or near the core-chain junctions of the bent-core molecules in either one or both the shorter *meta*- or the longer *para*-side of these asymmetric bent-shaped molecules imparts significant changes in the core-chain angle distributions and thus overall molecular conformation.[26] Basically, a chiral center residing at C-1 in the longer *para*-side, such as in compound **D**, leads to a significant shift to lower bend angles at the core-chain junction (resulting in the formation of heliconical-layered nanocylinders or HLNCs) compared to the larger bend angle at the core-chain junction calculated for compound **C** (forming helical microfilaments or HμFs), where the chiral center at C-1 is situated in the shorter *meta*-side (Figure 1a). Even then, as long as both core-chain junctions in the molecule feature a chiral center (and branching point) at C-1, dual-modulated HNFs are generated; with lower overall dimensions for the homochiral derivative **A** (HNF_{mod2a}) in comparison to **B** (HNF_{mod2b}) with alternating configuration of the chiral centers (Figure 1a).[20, 21]

Considering the established links between filament morphology and lowest-energy conformations affected by the distribution of dihedral angles in the core-chain junction,[26] the formation of flat or weakly twisted flat nanoribbons (FNRs or TNRs) when the chiral center(s) were relocated to C-2 (**E** and **F**, Figure 2a) seem a logical consequence. In line with earlier established trends for helical pitch (*p*) in chiral nematic (N*) phases or spontaneous polarization values in chiral smectic-C (SmC*) phases as a chiral center is moved further away from a core-chain juncture,[32] the formation of non-twisted, flat filaments, at least upon slow cooling from the isotropic liquid phase (at ~ 5 °C min^{-1}), is the result of a reduction of the restraint of rotation about the chiral center that effectively reduces the effects of chirality in the side chain. This is additionally supported by the fact that upon rapid cooling (at a rate ≥ 50 °C min^{-1}) conglomerates of left- and right-handed HNF_{mod2a} and HμF morphologies were seen for **E** and **F** (Figure 1a) despite the homochiral nature of the molecules.[28]

To further confirm that this trend holds up, the current work focuses on a new set of bent-core tris-biphenyl materials for which the chiral centers were further removed from the core-chain juncture, now to C-3. **BC1** – **BC4** have chiral centers at C-3 in both the *meta*- and *para*-arm. **BC1** is homochiral, featuring two (*R*)-3,7-dimethyloctan-1-olyl chiral side chains with a further branching point at the chain terminus—in analogy to **E** and **F**. **BC2** – **BC4** carry hexahydrofarnesolyl[33] groups in the side chains (two racemic side chains for **BC2** and one each in either

the longer *para*-arm for **BC3** or in the shorter *meta*-arm for **BC4** with the other side chain analogous to **BC1**). Finally, to probe the effect of mixed chiral center positions, **BC5** and **BC6** feature chiral centers at C-3 in the *para*-arm and C-1 in the *meta*-arm; homochiral (*R*,*R*)- for **BC5** and heterochiral (*R*,*S*)- for **BC6** (Figure 1b). Examining the self-assembly of these two derivatives will allow for a direct comparison with compound **E** featuring chiral centers at C-2 in either side chain.

Further insight into the role of low-energy conformations at the core-chain juncture will occur when we ultimately compare the final filament morphologies formed by **BC1**, **BC5**, and **BC6** (each with chiral centers at C-3) with those formed by compounds **E** (chiral centers at C-2; Figure 1a) and **G** (chiral centers at C-2 and C-3; Figure 2). In the case of **G**,[27] calculated conformational energy profiles revealed a greater conformational rigidity about the C-2–C-3 bond axis due to repulsive interactions of the two fluoro-substituents and the "*gauche* effect"[34] associated with this structural unit (i.e., hyperconjugative interactions between vicinal C–H and C–F bonds in the lowest energy conformation). As a result, no flat or weakly twisted nanoribbons were seen in this case, rather, a coexistence of HNF_{mod2b} and HLNC (Figure 2).

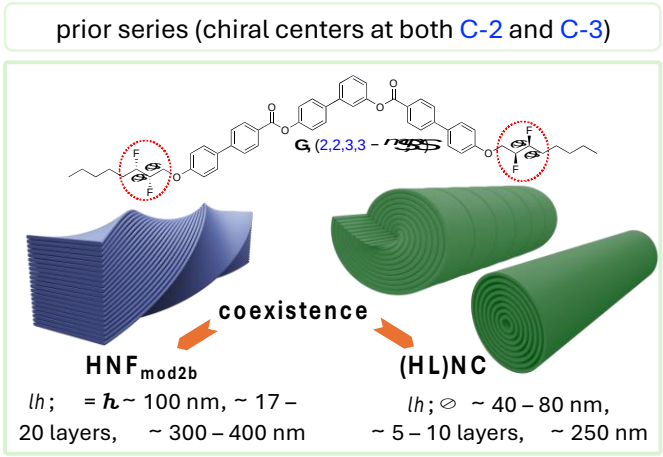

Figure 2. Bent-core molecule with chiral centers at C-2 and C-3 via the introduction of (*S*,*S*)-2,3-difluorooctyloxy side chains (compound **G**):[27] upon slow as well as rapid cooling, **G** showed a coexistence of two morphologies (HNF_{mod2b} and (HL)NC; heliconical layering was here only observed for some of nanocylinders (unlike for compound **D**; Figure 1, which showed heliconical layering depending on the configuration of the chiral center).

To clarify our expectations upfront for filament morphology due to the relocation of chiral centers in the core-chain junctures to C-3, we first proceeded to calculate the conformational energy profile about the C-2—C-3 bond along O—C-1—C-2—C-3 using DFT calculations (B3LYP/6-31G*).[35-37] Comparing the obtained energy profile with the ones previously calculated for related substructures with chiral centers either at C-1 or C-2 (Figure 3a) shows that chiral centers at C-3 impart similar conformational rigidity as chiral centers at C-1. The key difference appears to be that the residual aliphatic hydrocarbon chain now point in the opposite directions[28] for the same configuration of the chiral centers at C-1 and C-3 (see (*R*)-configuration plots and Newman projections in Figure 3b). In contrast, a chiral center at C-2 does not show preferential energy minimum for the two syn-clinical or the antiperiplanar lower-energy conformations (Figure 3b). Global energy minimum models of the core-chain substructure conformation with chiral center at C-3 nevertheless appear to show that this substructure is overall relatively linear with respect to the bent-core arm molecular substructure (Figure 3c) as was seen earlier for the substructure with the chiral center at C-2 (compounds **E** and **F** in Figure 1). Thus, the new derivatives with chiral centers exclusively at C-3 (**BC1** – **BC4**) should show a tendency for the formation of flat ribbon filaments due to the diminished effect of chirality when the chiral center is relocated even farther away from the core-chain juncture, the additional branching point at the chain terminus as for **E** and **F** (Figure 1), and the overall linear substructure conformation. However, the situation is more subtle for **BC5** and **BC6**. A chiral center at C-1 in the shorter *meta*-side should favor the formation of HμFs (as compounds **C** and **F**, Figure 1), but an additional chiral center in the longer *para*-side would perhaps lead to the formation of one of the other chiral morphologies (HNF or HLNC), in analogy to all other prior-series compounds (Figures 1 and 2).

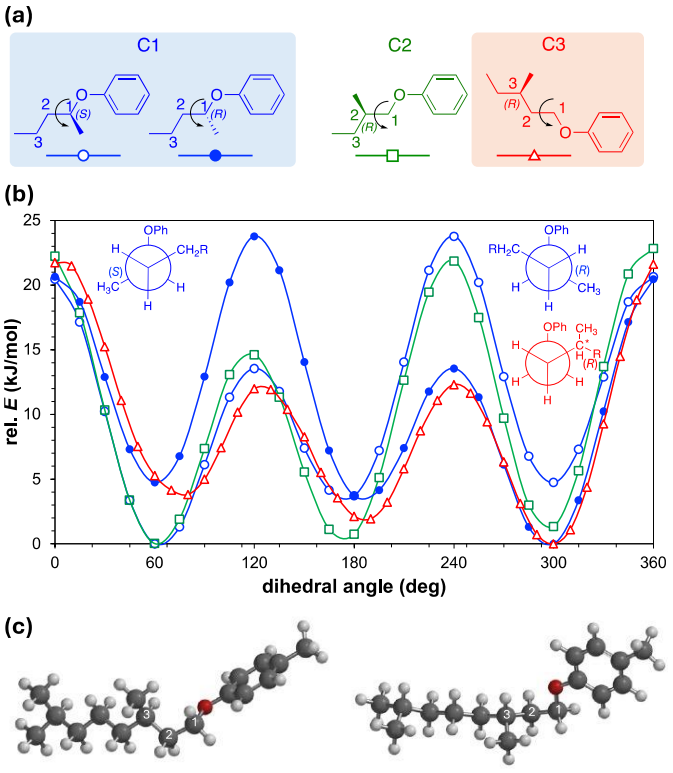

Figure 3. (a) Substructures of branched chiral side chains with chiral centers at C-1, C-2, or C-3 used for the calculation of the relative conformational energy profiles shown in (b). Newman projections for the two enantiomeric structures with chiral center at C-1 and for the (*R*)-enantiomer with the chiral center at C-3 are shown. (c) Two projections of the lowest energy conformation for the substructure with the chiral center at C-3.

Thus, to further advance our understanding of the role of chiral center relocation (away from the core-chain juncture) in these tris-biphenyl bent-core molecules and the ensuing molecular conformation on final filament morphology, all new-series compounds with chiral centers at C-3 or C-1 and C-3, **BC1** – **BC6**, were fully characterized by polarized optical microscopy (POM), differential scanning calorimetry (DSC), thin film circular dichroism (CD) spectropolarimetry, scanning and transmission

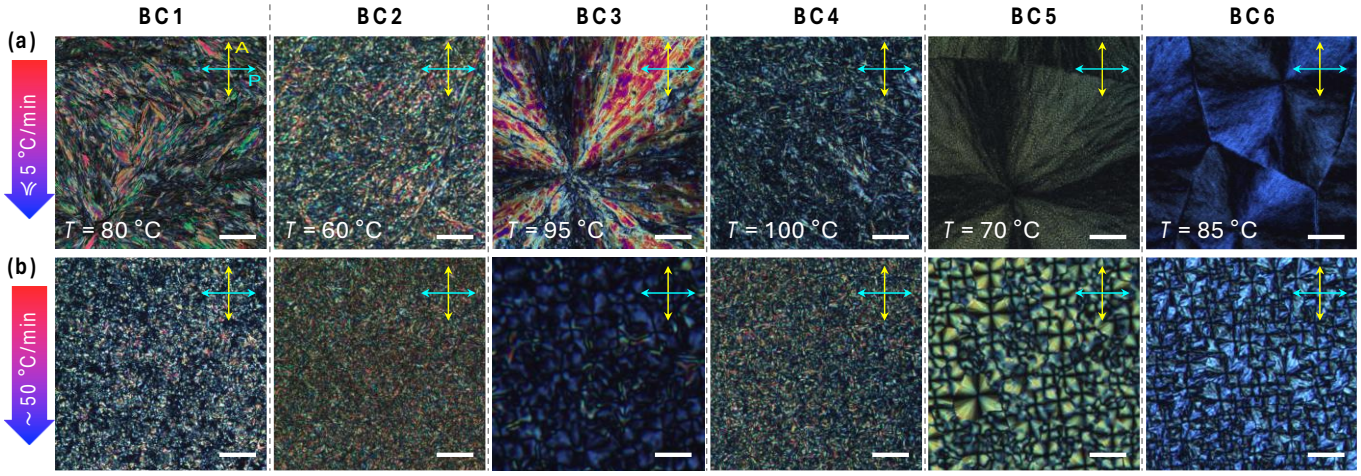

Figure 4. Polarized optical photomicrographs of **BC1** – **BC6** (crossed polarizer and analyzer) after heating to the isotropic liquid phase (i.e., >125 – 153 °C depending on clearing point of each compound) and subsequent: (a) slow cooling to room temperature at the cooling rate of <5 °C min^{-1} (temperature indicated) and (b) rapid cooling to room temperature (to $T \sim 20$ °C via rapid thermal quench) at a rate ≥50 °C min^{-1} (scale bars = 200 µm).

electron microscopy (SEM, TEM), and X-ray diffraction (XRD) both after slow and rapid cooling from the isotropic liquid.

2. Experimental

2.1 Materials

General and analytical methods as well as synthesis details and analytical data for intermediates and bent-core compounds **BC1** – **BC6** are given in the ESI (Section S1, Scheme S1, Figs. S1-S6).

2.2 Optical and thermal characterization

POM analysis and imaging were carried out using an Olympus BX-53 polarizing microscope equipped with a Linkam LTS420E heating/cooling stage. Samples were heated above the clearing point as indicated by DSC and then cooled at either <5 °C min^{-1} (commonly at 2 °C min^{-1}; slow cooling) or ≥50 °C min^{-1} (rapid cooling or thermal quench). The phase transition temperatures and enthalpies were measured using either a Perkin Elmer Pyris 1 DSC or a Perkin Elmer DSC-7 at two heating/cooling rates (either at 5 °C min^{-1} or at 50 °C min^{-1}), reporting data from the second heating/cooling runs, respectively. The temperature was calibrated with indium and zinc standards.

2.3 CD spectropolarimetry

For thin film CD measurements, to eliminate contributions from linear dichroism and birefringence, samples and sample areas were investigated at 45° interval sample rotation angles. The spectra were then summed up or averaged to provide genuine CD signals of the sample area.[20, 38] The area interrogated by the light beam, given by instrumental slit size and shape, is ~0.4 cm in diameter and larger than most individual domains seen by POM of the samples sandwiched between two untreated quartz substrates using nominal spacers of 10 µm.

2.4 Scanning and transmission electron microscopy

SEM analysis was performed using a Quanta 450 FEG SEM commonly without prior metal deposition. TEM was carried out on an FEI Tecnai F20 microscope, operating at 200 kV, and equipped with a Schottky field emission gun and a twin-blade anticontaminator. All images were recorded using a Gatan 4K Ultra Scan charge-coupled device camera. Since these organic material films are sensitive to electron beam irradiation, the films were normally previewed rapidly at a dose of 20 e^{-} nm^{-2}. Selected areas were then imaged at a dose level of 200 e^{-} nm^{-2}, which did not cause radiation damage. A drop of a solution of each compound in an organic solvent (CH_2Cl_2 or *n*-hexane) was placed either on indium tin oxide substrates for SEM or carbon-coated Cu grids for TEM imaging. After complete evaporation of the solvent in vacuum, samples were heated above the clearing point and cooled as described for the POM experiments, and then imaged. Image analysis was done using ImageJ®.[39]

2.5 X-ray diffraction

Variable-angle, temperature-controlled XRD experiments were performed with an in-house Xenocs Xeuss 3.0 using a Cu Kα source (λ = 1.54 Å) equipped with a Linkam HFSX350 heating-cooling stage. Samples were sealed into X-ray diffraction glass capillaries (Charles Supper Co.)

3. Results and discussion

3.1 Optical and thermal analysis

DSC data (ESI, Section S2, Figure S7, and Table S1) show that all compounds, except for **BC2**, show only one significant phase transition from the isotropic liquid phase on slow cooling (at a rate of 5 °C min^{-1}). **BC1** and **BC3**, assuming quasi-crystalline B4-type structures, show either one or several crystal-crystal phase transitions on cooling, respectively. **BC2**, in contrast, shows a phase transition on cooling at higher temperature characterized by a significantly lower phase transition enthalpy. Considering phase sequences frequently observed for prior series of tris-biphenyl bent-core derivatives, this could be a columnar phase, that, here, forms over a narrow (2 °C) temperature interval. On rapid cooling at 50 °C min^{-1}, **BC1** – **BC6** show only one obvious

phase transition (some with a discernable weak shoulder) and no glass transitions, often seen for B4-type bent-core materials, near room temperature.

POM studies performed next (see Figure 4) may provide further evidence about phase type or B4 morphology. Homochiral **BC1**, on slow cooling, displays a feather-like texture resembling, at least in overall appearance, the texture previously recorded for compound **E** on slow cooling.[28] Upon rapid thermal quenching to room temperature, though, the texture observed only shows smaller, grainy birefringent domains. Nearly identical textures were seen for **BC2** and **BC4** with racemic hexahydrofarnesolyl side chains either in both the *meta*- and the *para*-side or only in the shorter *meta*-side, respectively (**BC4** features a chiral center at C-3 in the longer *para*-side). The texture of the 2 °C wide, high temperature phase of **BC2** (ESI, Section S3, Figure S8) is best described as a broken spherulitic-type texture previously seen for columnar B1 phase, either neat or in coexistence with a B4-phase morphology.

In contrast, **BC3**, **BC5**, and **BC6** show textures on slow as well as rapid cooling that closely resemble the textures earlier reported for the various nano- and microfilament phases;[20-22, 28] bluish in appearance and with the usual focal conic- or spherulitic-like domains. Since these materials are non-racemic, uncrossing of polarizer and analyzer clock- or anticlockwise did not generate the darker and brighter domains that would reverse upon uncrossing the analyzer in the opposite direction[12] as for the chiral HNF conglomerates of achiral or racemic compounds (ESI, Section S3, Figure S9). Another typical feature seen in all sets of POM photomicrographs for these compounds are the smaller domains observed under the rapid cooling regime. Since no polymer alignment layers were used in these POM experiments (only plain, pre-cleaned glass slides), identical textures were seen for preparations between untreated quartz substrates used next for thin film CD spectropolarimetry.

3.2 Thin film CD spectropolarimetry

For practically all the previous nano- and microfilaments formed by these tris-biphenyl bent-core materials, sign and wavelength of the major bands in the thin film CD spectra provided a clear indication of the handedness and in many cases even the type of filament morphology. An analysis of the CD spectra measured for **BC1** – **BC6** (Figure 5) was significantly less straightforward. **BC1** on slow cooling showed individual CD spectra at the various sample rotation angles, all with weak positive bands centered around λ = 325 nm and a stronger negative band around λ = 350 nm. The sum CD signal is then similar with a positive as well as a negative band with maxima at these wavelengths; the latter one tailing off over a broad wavelength range (Figure 5a). The sum spectrum measured upon rapid cooling is similar. Here, only the intensities of the two sum maxima are reversed (Figure 5b). Both preparations with a nominal thickness of 10 µm, while weakly, show the distinctive bluish hue of the structural color commonly seen for B4 filament phases. The absence of a single clear maximum in these sum CD spectra already hints at a more complex, different, or the coexistence of more than just one morphology. The CD spectra of **BC2** and **BC3** (Figures 5c-f) are

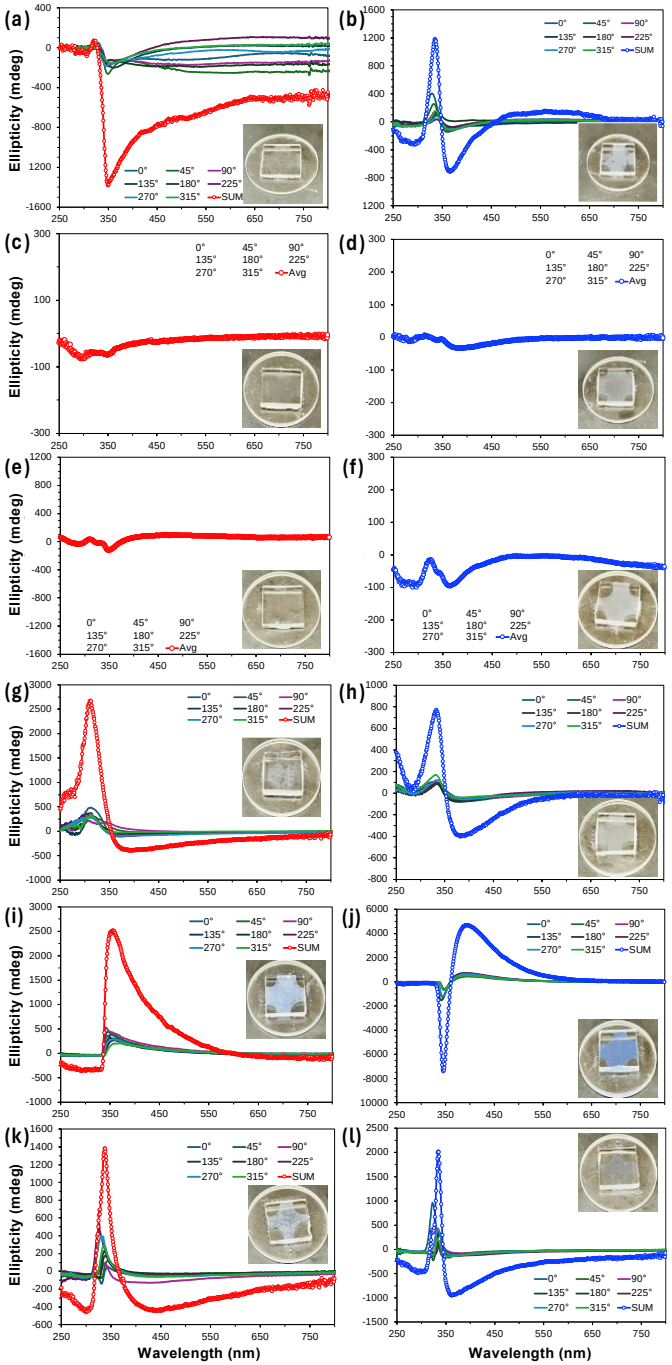

Figure 5. Thin-film CD spectra taken at 45° sample rotation angles ($\Delta\varepsilon$ [mdeg] vs. λ [nm]) of 10-µm films between untreated quartz substrates after cooling at a different rate from the isotropic liquid phase to room temperature (T ~ 20 °C) at different sample rotation angles as indicated in the legends (red SUM or average (Avg) datasets to cancel out linear dichroism and birefringence are for slow cooling (<5 °C min^{-1}); blue SUM or Avg datasets for rapid cooling (≥50 °C min^{-1})): (a, b) **BC1**, (c, d) **BC2**, (e, f) **BC3**, (g, h) **BC4**, (i, j) **BC5**, and (k, l) **BC6**. Insets in each graph are the sample photographs either showing or lacking blue structural color. Average rather than SUM spectra were generated from the individual 45° sample rotation datasets when the resulting graphs showed randomly positive or negative weaker signals over broader or specific spectral ranges (i.e., for **BC2** and **BC3**).

then even more puzzling and less clear. On both slow and rapid cooling from the isotropic liquid state, all individual 45° sample rotation spectra randomly show either positive or negative CD bands over the entire spectral region ranging from λ = 250 - 750

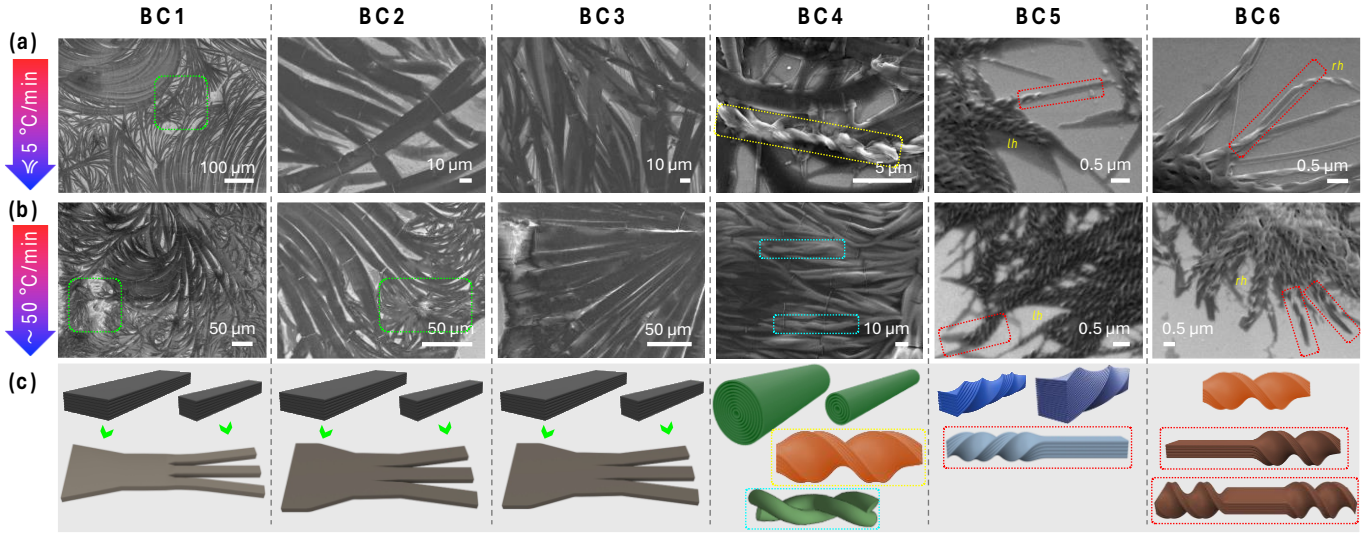

Figure 6. Representative SEM images obtained for **BC1** – **BC6**: (a) after slow cooling from the isotropic liquid state at a rate of <5 °C min^{-1} and (b) after rapid cooling (thermal quench) at a rate of ≥50 °C min^{-1}. (c) Schematic 3-D renderings depicting the morphologies seen in the SEM images. For additional SEM images of **BC4** see ESI, Section S4, Figure S10.

nm without any noteworthy sum-CD signal, which is why the average of these individual spectra is reported in these cases. Together with the lack of even a hue of blue structural color (see insets), these CD data would indicate that **BC2** and **BC3** do not form a chiral morphology under either cooling regime. For **BC4**, however, the situation reverses again, and sum-CD spectra like those collected for **BC1** (especially the sum-CD found on rapid cooling); a positive band centered near λ = 325 nm and a further negative band now centered at a longer wavelength around λ = 375 nm (Figure 5g and 5h). The relative similarity of the CD data for **BC4** and **BC1** may already indicate the presence of similar filament morphology for these two materials.

Finally, taking the comparatively intense blue structural color into account, it was not surprising that the CD spectra for **BC5** and **BC6** showed the most intense individual and sum-CD bands. On slow cooling, both compounds show intense positive sum-CD signals; centered around λ = 370 nm for **BC5** and around λ = 340 nm for **BC6** (Figure 5i and 5k). The identical positive sign of these CD bands on slow cooling is surprising considering the enantiomeric relationship of the involved chiral centers at C-1 in the shorter *meta*-side of these molecules, especially since the CD spectra taken on rapid cooling display the expected mirror relationship for enantiomeric species (Figure 5j and 5l), albeit at slightly different wavelength maxima. Given what we learned from CD data of prior series with diminished chirality due to chiral center relocation away from core-chain junctures, these CD datasets already indicate that we might see filaments of either handedness by electron microscopy.

3.3 SEM and TEM imaging

Initial observation of the filament morphologies formed upon slow or rapid cooling from the isotropic liquid by SEM revealed very similar filament types for **BC1** – **BC3** (Figure 6). Feather-like in appearance flat-looking filaments that curve almost look like split hair ends becoming finer, decreasing and further deceasing in width from $w \sim 10$ µm to less than 1 µm toward the filament ends. Moreover, the apparent curvature of these flat filaments appears to result in cracks, as indicated by white lines that run parallel to the filament widths. As the filaments become finer and finer towards their ends (e.g., highlighted areas with green boundary for **BC1** in Figure 6), SEM images were not able to resolve if any of the thinner flat filament endings twist. Twist would be particularly favorable for thinner flat filaments (here the ends), and potentially expected given that the constituent molecules have chiral side chains. Considering the formation of twisted nanoribbons (TNRs) upon slow cooling and both left- and right-handed filaments upon rapid cooling by the closest relative in prior series, i.e., compound **E** with chiral centers at C-2 (Figure 1), we expected to see a similar behavior at least for **BC1**, given: (1) that the thin film CD spectra (Figures 5a,b) show clear negative (slow cooling) as well as negative and positive sum-CD bands (rapid cooling), (2) the faint but present blue structural color (insets, Figures 5a,b), and (3) the lowest energy conformation of the BC molecules with a chiral center at C-3 that seems more closely related to those with a chiral center at C-1 (forming HNFs)[20] than at C-2 (forming FNRs[28] among other morphologies).

BC4, despite all its structural similarity to **BC1** – **BC3**, however, forms two rather different morphologies, as can be seen in the SEM images (Figure 6). One of the two morphologies, with similar features and overall dimensions on both slow and rapid cooling, and again splitting increasingly finer filaments, appears rather cylindrical with a spherical cross-section (and a diameter ranging from ⌀ ~ 200 nm – 2 µm) rather than flat as for **BC1** – **BC3**. Assuming a nanocylinder-like morphology, no helicoidal wrapping of the outer layer is seen, as first reported for **D** (Figure 1)[26] with a chiral center at C-1 in the longer *para*-side. A similar lack of helicoidal wrapping, however, was reported for a homologue of **D** with longer aliphatic chains and a chiral center at *para*-C-1[28] and **G** with chiral centers at C-2 and C-3[27] (Figure 2). As seen before for **D**, these cylinder-like morphologies braid (wrap around one another) as revealed in the highlighted area with turquoise boundary upon rapid cooling. The other clearly discernable morphology formed by **BC4** exclusively upon slow

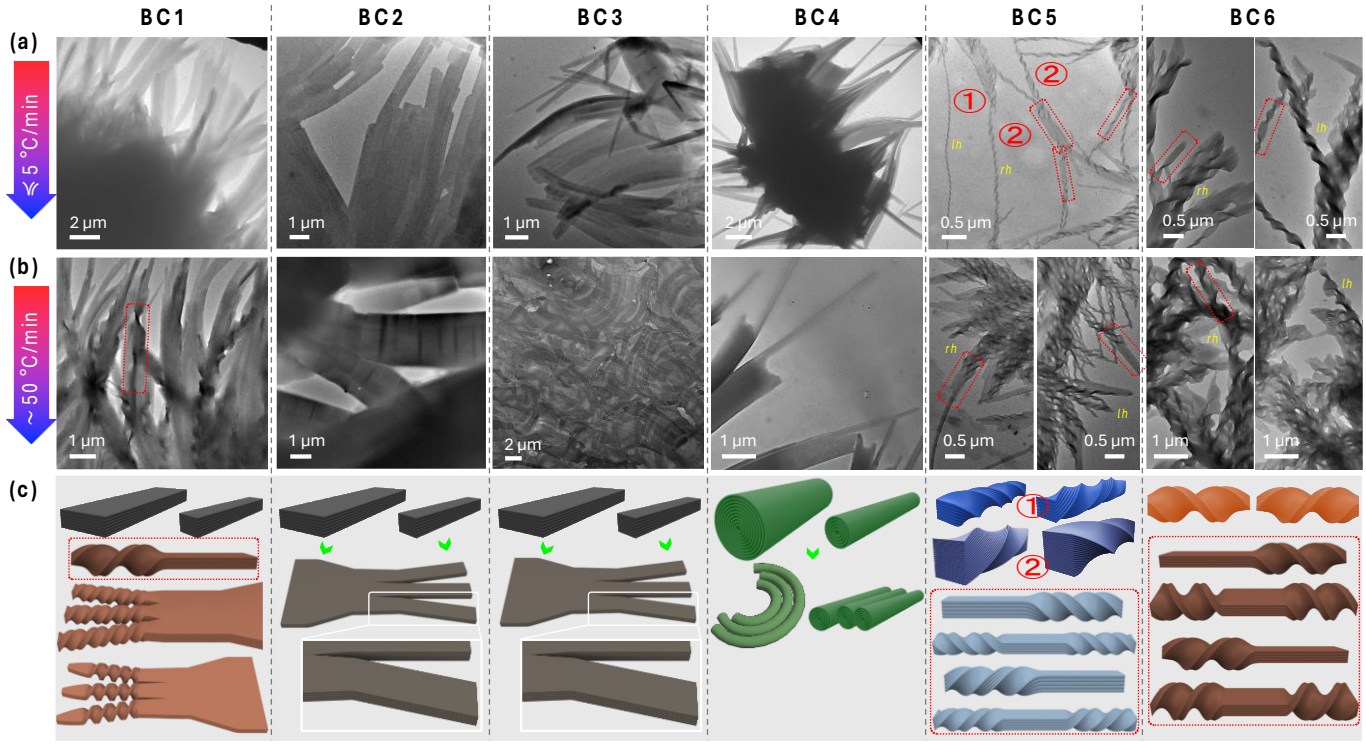

Figure 7. Representative TEM images obtained for **BC1** – **BC6**: (a) after slow cooling from the isotropic liquid state at a rate of <5 °C min^{-1} and (b) after rapid cooling (thermal quench) at a rate of ≥50 °C min^{-1}. (c) Schematic 3-D renderings depicting the various morphologies seen in the TEM images. For additional TEM images of **BC1**, **BC5**, and **BC6** see ESI, Section S4, Figures S11 – S16.

cooling is those of twisted microfilaments with dimensions of $w \sim 900$ nm and $p \sim 3.5$ to 4 µm (highlighted area with yellow boundary in Figure 6 and ESI, Section S4, Figure S10), i.e., just about fourfold larger than the HµFs formed by **C** and **F** (Figure 1).[22, 28] In line with the positive sign of the sum-CD band (Figure 5g), these somewhat isolated HµFs are all right-handed.

Finally, once the chiral center in the shorter *meta*-side relocates back from C-3 to C-1, the morphology observed by SEM changes again. However, before stressing the differences between the filaments formed by **BC5** and **BC6** regarding type, handedness, and dimensions, a common filament feature not seen before is a change in the morphology within one and the same filament. Seen for both **BC5** and **BC6** upon slow as well as rapid cooling, twisted filaments suddenly unwind to form flat ribbons. Most of these twisted filaments unwind at the ends; some show shorter unwound flat segments, which then twist again with the identical twist sense (see highlighted areas in Figure 6 with red boundaries). Twisted sections of the filaments formed by **BC5** show smaller width and pitch ($w \sim 100 - 180$ nm, $p \sim 300 - 450$ nm) than those formed by **BC6** ($w \sim 300$ nm, $p \sim 900$ nm). Thus, twisted sections of **BC5** should be considered HNFs in analogy to the HNF$_{mod2b}$s formed by **B** (Figure 1);[21] those of **BC6** HµFs in analogy to **C** (Figure 1).[22] The filaments with larger width clearly visible for **BC5** in the SEM images are predominantly left-handed—in contrast to the positive sum-CD band recorded by CD on slow cooling (Figure 5i) but in line with the sign of the first sum-CD signal on rapid cooling (Figure 5j). The handedness of the HµFs formed by **BC6** (right-handed) is in line with the sum-CD bands seen upon slow and rapid cooling (Figures 5k and 5l) but in contrast to the configuration of the chiral center at C-1 in the shorter *meta*-side of the molecule compared to **C** (Figure 1). **C** featuring a chiral center at C-1 with (*R*)-configuration formed solely right-handed HµFs.[22] So, assuming that a chiral center at C-1 should be the more dominating factor in deciding filament handedness, given that chirality diminishes as the chiral center is relocated farther away from the core-chain juncture, **BC6** having an (*S*)-configuration chiral center at C-1 in the *meta*-side should form left-handed HµFs. Considering the images shown in Figure 7, however, TEM data for **BC1** – **BC6** provided far more clarity on the types and specific filament shapes.

Significantly, TEM imaging revealed that among the smaller flat filaments formed by **BC1**, which could not be clearly resolved by SEM, several of those with smaller widths do eventually twist at the ends. As predicted by theory,[40-42] multilayer filament twist is energetically only favorable for lower filament heights and more narrow widths, which is exactly what is observed for **BC1**. Wider flat ribbons branch into narrower ones, which twist at the ends (Figure 7c). Some, as seen for **BC5** and **BC6** by SEM imaging, also show flat (untwisted) segments between two twisted ones (area highlighted with a red boundary for **BC1** in Figure 7b). Most of the filaments, however, as already seen in the SEM images, are FNRs with many of the narrow filaments showing values of $w \sim 450$ nm (since those could now be imaged by TEM). Further supporting the just-made argument about the correlation between width and the probability for twist, dimensions of the twisted filament branches, almost identical under either cooling regime, are consistently smaller, with $w \sim 400$ nm and $p \sim 2$ µm. Thus, the twisted filament ends are HµFs with dimensions about twofold larger than those initially reported for **C** (Figure 1), likely a consequence of the

diminished chirality when the chiral centers are moved farther away from the core-chain juncture, as predicted earlier. After slow cooling, filaments are primarily left-handed, as shown in Figure 7 and the ESI (Section S4, Figure S11), in line with the negative sum-CD band centered around $\lambda \sim 350$ nm for **BC1** (Figure 5a). After rapid cooling, mostly left- but also isolated right-handed filaments can be seen by TEM (ESI, Section S4, Figure S12), again in line with the thin film CD data (Figure 5b).

For **BC2** and **BC3**, TEM confirmed the flat ribbon nature, simply adding that the width can be as low as a few hundred nm (as low as $w \sim 300$ nm), however, without any visible twist even for the narrowest filaments.

For **BC4**, TEM allowed for a better visualization of nanocylinders (NCs) with smaller diameters, now as low as $\oslash \sim 130 - 180$ nm (Figures 7a and 7b), which often bundle into three-dimensional constructs (Figure 7a), quite like those reported previously for **D** (Figure 1).[26] While the nanocylinder-type nature is more challenging to recognize in TEM images, several do show cross-sectional electron density profiles (i.e., darker-brighter-darker) comparable to those we reported earlier for **D**,[26] possibly even suggesting a hollow inner core.

Finally, for **BC5** and **BC6**, both types and dimensions of filaments imaged by TEM drastically changes in comparison to **BC1** – **BC4**. The first obvious difference is the overall much smaller filament dimensions seen for **BC5** and **BC6**, as already seen by SEM. The second obvious difference is that the TEM images now show a more intricate mix of filament types and dimensions. Moreover, many filaments display a change in morphology along one and the same filament, hinted at by SEM. For **BC5**, both left- and right-handed twisted filaments can be seen, some with dimensions of $w \sim 40$ nm and $p \sim 240$ nm as HNF_{mod2a} formed by **A** and **E** (Figure 1), some with dimensions of $w \sim 70 - 120$ nm and $p \sim 320 - 550$ nm more similar to the HNF_{mod2b} formed by **B** (Figure 7 and ESI, Section S4, Figures S13 & S14). The potential presence or absence of further intra- or interlayer modulations will be clarified by XRD in the next section. Notably, HNFs with smaller widths form upon slow cooling from the isotropic liquid. Under each cooling regime, many twisted filaments (in some areas almost all) are unwound, forming FNRs at the ends, while several twisted filaments flatten for sections as long as 500 nm, only to twist again with the same twist sense (Figure 7 and ESI, Section S4, Figure S13), i.e., without perversions. The filaments formed by **BC6** share almost all these traits with the one exception that these filaments are larger. With an average width of $w \sim 240 - 280$ nm and a pitch of $p \sim 950$ nm (Figure 7 and ESI, Section S4, Figures S15 and S16), these filament should be considered HμFs in analogy to those formed by compounds **C** and **F** (Figure 1). The evident random change of handedness in the TEM images also makes a meaningful correlation with the thin film CD data challenging (Figures 5i-l). The (*R*)-configuration at C-1 for **BC5** (assuming this to be the 'dominant' chiral center) should lead to right-handed HNFs and positive CD bands, the (*S*)-configuration at C-1 for **BC6** to left-handed HNFs and thus negative CD bands considering a comparison to compound **A**.[20] However, prior studies on compounds with mixed configuration on either side at C-1 suggested that the opposite configuration of the two chiral centers leads to larger filament dimensions (as for **BC6** in comparison to **BC5** in the current series). To confirm the crystalline lamellar nature (i.e., B4-type) and any potential intra- or interlayer modulation within the filaments formed by **BC1** – **BC6**, we performed XRD measurements both after slow and rapid cooling from the isotropic liquid state.

3.4 X-ray diffraction data

All B4 morphologies discovered so far are based upon lamellar structures—layers that are either flat, twisted, or writhed. Yet, the global molecular conformation of the constituent bent-core molecules governs local packing and thus internal structure. Accordingly, each B4 morphology discovered to date has been characterized by, or better, originated from a distinct molecular packing (incl. in-layer tilt and intra- or interlayer modulations), ultimately giving rise to distinct X-ray diffraction patterns.[20-22, 27, 28] Thus, given the coexistence of several morphologies or morphological evolutions detected by electron microscopy we should expect reasonably complex XRD patterns for **BC1** – **BC6**. Figure 8 shows all medium-angle XRD (MAXD) patterns ($q \sim 0.1 - 0.7$ Å^{-1}) for **BC1** – **BC6**; diffraction patterns covering also the wide-angle (WAXD) region as well as peak listings, relative intensities, peak deconvolution, peak fitting, and Miller indices are provided in the ESI (Section S5, Figures S17 – S30).

BC1 showed the coexistence of FNRs either varying in width or splitting into finer and finer FNRs with gradually lower widths as well as HμFs that occasionally unwind at the ends. **BC1**, as a result thereof, then produces an XRD pattern where upon slow (Figure 8a) as well as upon rapid cooling to room temperature (Figure 8b) three sets of (00l) diffraction peaks with l = 1, 2, … can be indexed (q_1^a = 0.165 Å^{-1}, q_1^b = 0.174 Å^{-1}, and q_1^c = 0.181 Å^{-1} on slow cooling and q_2^a = 0.167 Å^{-1}, q_1^b = 0.137 Å^{-1} and q_1^c = 0.169 Å^{-1} on rapid cooling; for the corresponding higher-order reflections, q_n^x with n = 2,3 and $x = a - c$ see ESI, Section S5, Figures S17 and S18, and Tables S2 and S3). One of the two structures seen upon rapid cooling is clearly a modulated layer structure with $q_3^a = ({q_1^a}^2 + {q_2^a}^2)^{½}$. The q values for the (001) reflections then indicate variable layer spacings for each morphology, ranging from d = 3.81 – 3.47 nm upon slow cooling and d = 4.58 nm and d = 3.72 nm upon rapid cooling, driven by variations in molecular tilt within the layers from $\theta \sim 13°$ for one of the structures seen upon rapid cooling to 42° for one detected upon slow cooling, given a calculated molecular length of l = 4.7 nm. Given the spatial heterogeneity of coexisting morphologies seen by SEM and TEM, it seems not surprising that interrogating another sample location by XRD (realized by moving the X-ray capillary within the hot stage) revealed coexistence with yet another structure (ESI, Section S5, Figure S19 and Table S4) on rapid cooling. This subset of diffraction maxima q_i (i = 1, ..., 10) is best indexed as (001), (100), (010), (101), (111), (002), (200), (11$\bar{2}$), (020), and (120) with an oblique lattice and monoclinic space group *P*2 (3D), as shown in the ESI (Section S5, Figure S19, Table S4). The calculated lattice parameters of this 3D Col_{ob}–*P*2 phase are a = 40.2 Å, b = 34.9 Å, c = 42.4 Å, and β = 102°. Similar phase coexistences as seen here for **BC1** upon rapid cooling (B1 Col_{ob}–*P*2 phase; structure shown in ESI, Figure S19) have previously been reported for

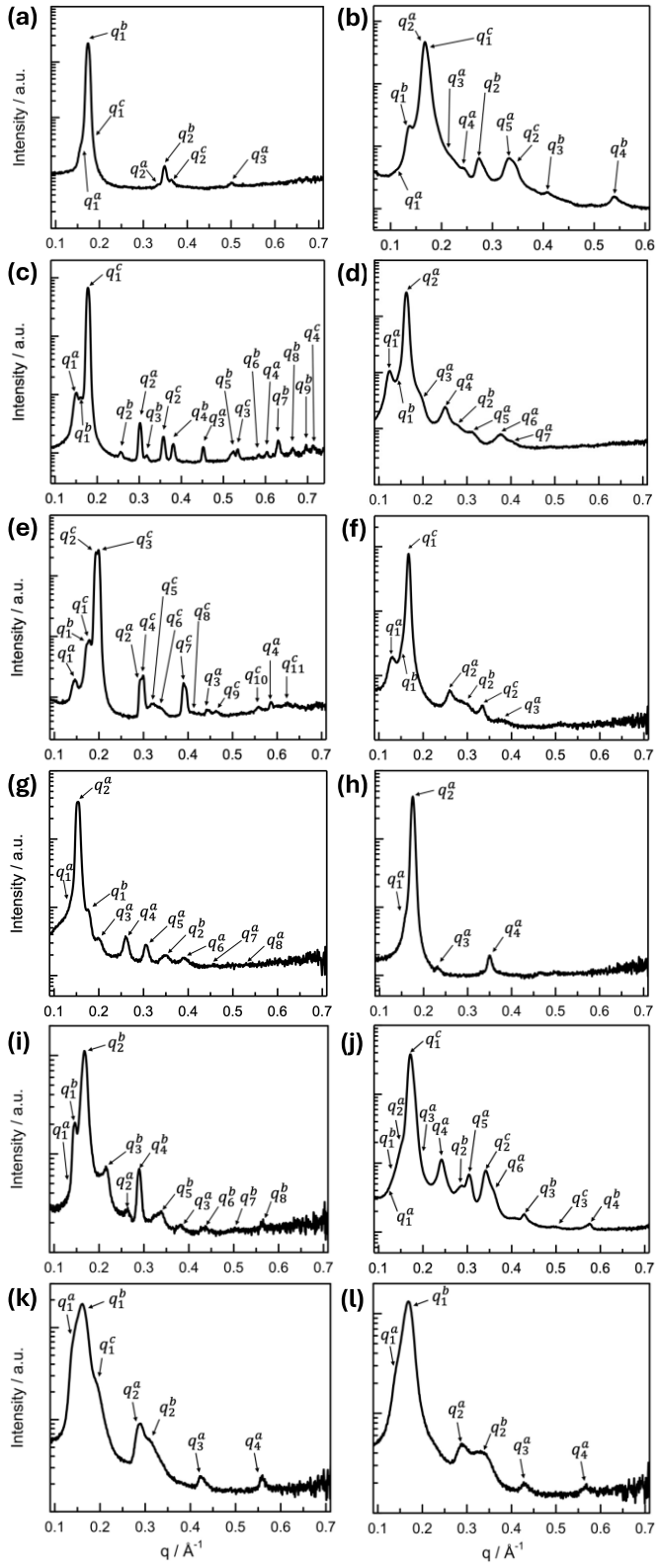

Figure 8. XRD analysis data showing intensity (a.u.) vs. wave vector q (Å^{-1}) of the MAXD region: (left column) slow cooling and (right column) fast cooling. (a, b) **BC1**, (c, d) **BC2**, (e, f) **BC3**, (g, h) **BC4**, (i, j) **BC5**, and (k, l) **BC6**. Peak positions, relative intensity values, and Miller indices are provided in the ESI, Section S5, Figures S17 – S30, Tables S2 – S15.

other compounds in prior reported tris-biphenyl series.[28]

For **BC2**, upon slow cooling, a phase coexistence was observed between two non-modulated B4 structures and a B1 Col$_r$–$c2mm$ phase (Figure 8c). The two B4 structure sets of (00l) diffraction peaks with l = 1, …, 4 were identified with q_1^a = 0.151 Å^{-1} and q_1^c = 0.178 Å^{-1}. The corresponding higher-order reflections, q_n^x with n = 2 - 4 and $x = a, c$ are given in the ESI, Section S5, Figure S20 and Table S5. The q values for these 001 reflections indicate layer spacings for the two morphologies, likely the wider and narrower FNRs, of d = 4.16 nm (q_1^a series) and d = 3.53 nm (q_1^c series), again associated with variations in molecular tilt within the layers of $\theta \sim 39°$ or 49°, respectively, taking into account a calculated molecular length of **BC2** of l = 5.4 nm. A third set of diffraction peaks labeled $q_1^b - q_9^b$ were indexed as (001), (101), (002), (102), (103), (301), (203), (104), and (302) signifying a rectangular lattice with $c2mm$ plane group (2D) and lattice parameters of a = 31.4 Å and c = 39.0 Å, in which the molecules with highly branched side chains tilt significantly—a carry-over from a phase transition seen by DSC (ESI, Figure S7c). On rapid cooling, **BC2** shows only two B4 structures (Figure 8d). One is a modulated layer structure with $q_3^a = ({q_1^a}^2 + {q_2^a}^2)^{½}$ and maxima at q_1^a = 0.123 Å^{-1}, q_2^a = 0.161 Å^{-1}, and q_3^a = 0.202 Å^{-1}; values for the other reflections indexed as (200), (002), (300), and (202) are given in the ESI (Section S5, Figure S21, Table S6). The second structure is non-modulated with q_1^b = 0.139 Å^{-1} and q_2^b = 0.278 Å^{-1}. The layer spacing of the modulated phase amounts to d = 5.11 nm (indicating a tilt of the molecules within the layer of $\theta \sim 19°$); the non-modulated phase layer spacing is d = 4.52 nm from which a molecular tilt of $\theta \sim 33°$ can be calculated.

Relatively similar phase coexistences were again found for **BC3**, not unpredicted given the similarity in coexisting morphologies seen by electron microscopy. After slow cooling, **BC3** exhibits diffraction maxima (Figure 8e) best assumed to be from two non-modulated B4 structures with layer spacings of d = 4.33 nm (q_1^a series) and d = 3.65 nm (q_1^b series)—assuming a calculated molecular length of l = 5.1 nm and tilt angles $\theta \sim 32°$ and 44°, respectively, in addition to a coexisting B1 Col$_{ob}$-$P2$ (3D) phase (similar to **BC2** upon rapid cooling) with somewhat similar lattice parameters of a = 32.7 Å, b = 31.6 Å, c = 35.3 Å, and β = 102° (ESI, Section S5, Figure S22, Table S7). Upon rapid cooling, a somewhat simpler diffraction pattern indicates the formation of three non-modulated filament structures for **BC3** indexed with three sets of (00l) reflections (l = 1-3), i.e., lamellar structures with layer spacings of d = 4.87, 4.16 and 3.76 nm and tilt angles ranging from $\theta \sim 17°$ to 42° (Figure 8f and ESI, Section S5, Figure S23, Table S8). **BC3** is the only compound in this series that forms a high temperature phase above the B4 phase (see DSC data in the ESI, Figure S7e). Considering the coexisting B1 Col$_{ob}$-$P2$ phase seen upon slow cooling, unsurprisingly, this high-temperature phase is also a B1 Col$_{ob}$-$P2$ (3D) phase with lattice parameters of a = 37.1 Å, b = 33.2 Å, c = 41.8 Å, and β = 102° that are slightly larger as a result of this phase being observed at a temperature range between T = 139 to 142 °C on heating (ESI, Figure S24, Table S9).

For **BC4**, considering that we only observed two morphologies upon slow cooling (NCs and HμFs) and just NCs on rapid cooling, expectations were that the X-ray diffraction pattern will confirm this. Indeed, upon slow cooling, **BC4** shows the coexistence of a modulated and a non-modulated B4 structure (Figure 8g). The

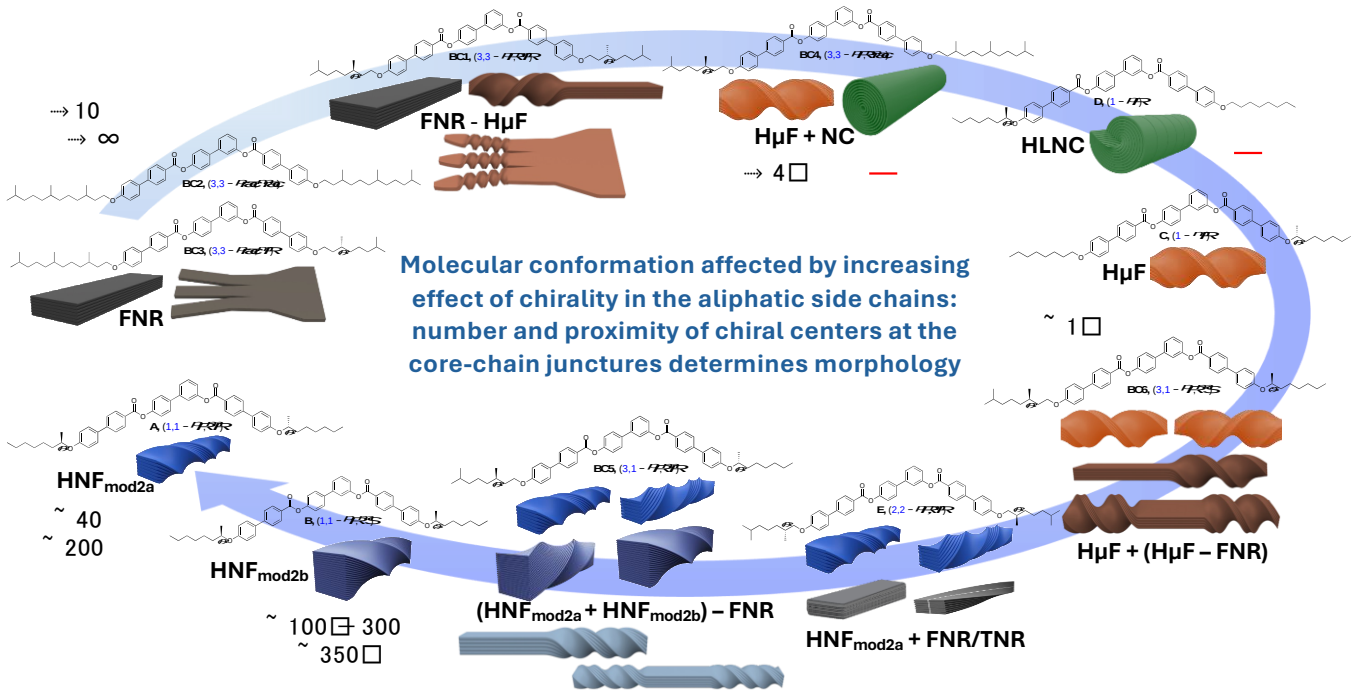

Figure 9. Evolution of B4 morphologies discovered to date depending on the increasing effect of chirality in the side chains near or at the core-chain juncture(s)—precisely the number and position of the chiral centers—from flat nanoribbons (FNRs) formed by **BC1** – **BC3** with branching points and chiral centers at C-3 over microfilaments and nanocylinder morphologies for single chiral centers at C-1 to the helical nanofilaments formed by **BC5**, **A**[20], and **B**[21], with chiral centers at C-1.

modulated layer structure features $q_3^a = (q_1^{a\,2} + q_2^{a\,2})^{½}$ and maxima at q_1^a = 0.130 Å^{-1} (100), q_2^a = 0.153 Å^{-1} (001), and q_3^a = 0.200 Å^{-1} (101). The values for the other reflections indexed as (200), (002), (300), (003), and (400) are given in the ESI (Section S5, Figure S25, Table S10). The layer spacing of this morphology is d = 4.10 nm and the tilt $\theta \sim 36°$ considering the calculated molecular length of l = 5.1 nm. The non-modulated structure shows (00l) reflections with l = 1, 2, and 4 with q_1^a = 0.172 Å^{-1} (001) and thus a layer spacing of d = 3.65 nm and a larger tilt of $\theta \sim 44°$ (ESI, Section S5, Figure S25, Table S10). Given that the single structure seen upon rapid cooling is also modulated, we assume that the NC morphology seen by electron microscopy after both cooling regimes is the one with the modulated structure. The layer spacing is d = 3.57 nm and the tilt $\theta \sim 45°$ (Figure 8h and ESI, Section S5, Figure S26, Table S11).

BC5, which forms smaller HNF$_{mod2a}$s and larger HNF$_{mod2b}$s that intermittently or at the ends untwist, as seen in the electron micrographs, shows complex diffraction patterns that confirm the presence of multiple coexisting morphologies as well. Upon slow cooling, a modulated and a non-modulated B4 structure were assigned with q_1^a = 0.134 Å^{-1} and q_2^b = 0.166 Å^{-1} (Figure 8i). The corresponding higher-order reflections, q_n^x with n = 3 or 8 and $x = a, b$ are given in the ESI (Section S5, Figure S27, Table S12). The modulated layer structure according to $q_3^b = (q_1^{b\,2} + q_2^{b\,2})^{½}$ features a layer spacing of d = 3.79 nm and a molecular tilt of $\theta \sim 34°$ considering a calculated molecular length of l = 4.6 nm. The non-modulated B4 structure is quasi non-tilted with a layer spacing of d = 4.67 nm that near matches the molecular length of **BC5**. Upon rapid cooling of **BC5**, three coexisting B4 structures were identified in the diffraction pattern (Figure 8j). Again, one is modulated, and the other two non-modulated. The (001) reflections for the two non-modulated structures at q_1^b = 0.143 Å^{-1} and q_1^c = 0.172 Å^{-1} provide values for the layer spacing of d = 4.39 and d = 3.65 nm and thus tilt angles of $\theta \sim 17°$ and $\theta \sim 37°$, similar to the values calculated for other morphologies formed by **BC1** – **BC4**. The modulated structure with $q_3^a = (q_1^{a\,2} + q_2^{a\,2})^{½}$ has a layer spacing of d = 4.11 nm and a tilt of $\theta \sim 27°$ (values for higher order reflections are given in the ESI, Figure S28, Table S13).

Finally, **BC6**'s diffraction pattern upon slow cooling revealed three non-modulated B4 structures with q_1^a = 0.143 Å^{-1}, q_1^b = 0.159 Å^{-1}, and q_1^c = 0.185 Å^{-1} (layers spacings ranging from d = 4.39 – 3.40 nm and tilt angles of $\theta \sim 17°$, 31°, and 42°), and upon rapid cooling two non-modulated B4 structures with q_1^a = 0.146 Å^{-1} and q_1^b = 0.169 Å^{-1}, and thus, each with very similar values for d and θ to two seen on slow cooling (d = 4.30 nm, $\theta \sim 21°$ and d = 3.72 nm, $\theta \sim 36°$). For values of higher order reflections, see ESI (Figures S29 and S30, Tables S14 and S15).

Overall, analysis of the complex XRD patterns further supports what was already suggested by the thin film CD data and clearly seen by EM imaging. The local packing of the molecules in layers affected by the overall molecular conformation via the presence of strategically placed chiral centers and their configuration, and further, additional branching points in the side chains, leads to frustration that globally manifests itself in the formation of coexisting nano- and microscale filament morphologies. While we cannot assign sets of specific internal structural features to any particular morphology, differences in local packing clearly control what overall morphologies are formed by **BC1** – **BC6**. Figure 9 and Table 1 summarize the overall findings, highlighting trends with respect to filament type and dimensions as well as dimensions (d, θ) of the internal structure.

Table 1. Summary of filament morphologies, dimensions and handedness as well as parameters of the underlying structures of the nano- and microfilaments formed by **BC1** – **BC6**.

#	cooling regime	morphologies	dimensions	handedness	layer spacing d (nm)	tilt angle θ (°)	structural color
BC1	*SC*	(FNR_{wide}—FNR_{narrow}—HμF)	FNR—: $w = h$ <1 – 10 μm —HμF: $w \sim 400$ nm $p \sim 2$ μm	*lh*	3.81 – 3.47	13 – 42	No
	FC	(FNR_{wide}—FNR_{narrow}—HμF)$_{(mod)}$ + Col_{ob}–*P*2			4.58 – 3.72		Yes
BC2	*SC*	(FNR_{wide}—FNR_{narrow}) + Col_r–*c*2*mm*	$w \sim$ <1 – 10 μm	N/A	4.16 – 3.53	39 – 49	No
	FC	(FNR_{wide}—FNR_{narrow})$_{(mod)}$			5.11 – 4.52	19 – 33	No
BC3	*SC*	(FNR_{wide}—FNR_{narrow}) + Col_{ob}–*P*2	$w \sim$ <1 – 10 μm	N/A	4.33 – 3.65	32 – 44	No
	FC	FNR_{wide}—FNR_{narrow}			4.87 – 3.76	17 – 42	No
BC4	*SC*	NC_{mod} + HμF	NC_{mod} ⌀ ~ 0.13 – 2 μm		4.10	36	Yes, weak
			HμF $w \sim 900$ nm, $p \sim 3.5 – 4.0$ μm	*rh*	3.65	44	
	FC	NC_{mod}	⌀ ~ 0.13 – 2 μm		3.57	45	Yes, weak
BC5	*SC*	[HNF_a + HNF_b + HNF_a—FNR—(HNF_a) + HNF_b-FNR-(HNF_b)]$_{(mod)}$	HNF_a: $w \sim 40$ nm, $p \sim 240$ nm HNF_b: $w \sim 70 – 120$ nm, $p \sim 320 – 550$ nm —FNR: $w \sim 40 – 120$ nm	*lh* & *rh*	4.67 – 3.79	0 – 34	Yes
	FC				4.39 – 3.65	17 – 37	Yes
BC6	*SC*	HμF + HμF—FNR—(HμF)	HμF—: $w \sim 240 – 280$ nm, $p \sim 950$ nm —FNR: $w \sim 240 – 280$ nm	*lh* & *rh*	4.39 – 3.40	17 – 42	Yes
	FC				4.30 – 3.72	21 – 36	Yes

Abbreviations/symbols: *SC* = slow cooling (5 °C min^{-1}), *FC* = fast cooling (≥50 °C min^{-1}), *lh* = left-handed, *rh* = right-handed, **+** sign = coexisting morphologies, morphology—morphology = progressive changes in morphology, mod = modulated (i.e., intra-layer modulation), (mod) = modulation observed for some but not all the coexisting morphologies, N/A = not applicable.

4. Conclusions

As graphically recapitulated in Figure 9, the set of asymmetric tris-biphenyl bent-core compounds discussed here, **BC1** – **BC6**, fully closes the circle from flat non-twisted to helical multilayer ribbons with the smallest possible physical dimensions (width, height, and helical pitch). As reviewed recently in this journal,[10] inter- or intralayer misfits caused by anisotropic multi-layer configurations, templating, packing frustration, amphiphilicity, intrinsic chirality, or specific molecular conformations imposing supramolecular chirality ultimately generate twisted or writhed flat ribbons. Combined with our earlier work, we here show that intralayer misfits and thus the ensuing nano- or microfilament shapes and dimensions can be predicted and engineered by strategically incorporating chiral centers/branching points into the aliphatic side chains. The most critical structural parameters to adjust for such predictable morphology engineering are the number and configuration of chiral centers as well as their exact position within the core-chain juncture (now altered from C-1 to C-3 in the alkyloxy side chains). All morphologies previously reported, even in cases of coexisting morphologies, adopted a specific morphology, either separately or along with another morphology. In the present series, **BC2** and **BC4** are examples of this type of behavior. In some instances, the cooling rate, either slow or rapid, decided which morphology (phase) was formed or coexisted (e.g., compounds **C** – **F**, Figure 1). **BC3** in the current series is another example of this cooling rate dependence.

In stark contrast, **BC1**, **BC5**, and **BC6** exhibit clear morphological transformations within one and the same filament. **BC1** forms flat multilayer ribbons that initially and progressively lessen in width to ultimately twist at the ends when a lower threshold of width is reached. Accordingly, **BC1** serves as a unique example and visual glimpse (quasi as a still image of a nonexistent movie) in support of the earlier discussed relationship between limited filament width and height that lends itself to energetically favorable twist. Comparable gradual shape evolutions have previously been reported only for very few materials such as peptide amphiphiles.[43] The reduced effect of chirality when the chiral centers are relocated from C-2 (as for compound **E**, Figure 1) to C-3, according to Gray and McDonnell rules,[44] is visually apparent by comparing the dimensions of the twisted filaments (HNFs formed by **E** exclusively upon rapid cooling and HμFs by **BC1**). Yet, the more pronounced conformational bias toward one conformation when the chiral center resides at C-3 (Figure 3b) leads to the formation of only one handedness for the HμFs at the filament ends seen for **BC1**.

BC5 and **BC6** with mixed positions of the chiral centers near the core-chain junctures (C-1 and C-3) show another type of shape evolution. Here, twisted filaments (varying in width/height) are untwisted either somewhere along the filament and/or at their ends. In each case, and in analogy to **E** with chiral centers at C-2, both left- and right-handed filaments form simultaneously. Surprisingly then, that not a single one of the filaments showed a perversion[45] (i.e., a change in handedness before and after a flat ribbon section). We assume that the intrinsic chirality of the molecules and their asymmetric overall structure prevent the conservation of zero overall twist. Lastly, again in analogy to other compounds in the series, **BC5**, with identical (homochiral) configuration of the two chiral centers, forms filaments with smaller dimensions (HNF_a and HNF_b), while **BC6** with alternating chiral center configuration forms HμFs (see Table1). The same behavior was earlier reported for compounds **A** and **B** (Figure 1 and Figure 9) forming smaller HNF_{mod2a} and larger HNF_{mod2b},

respectively.[20, 21] Overall, our expansion of the series discussed here highlights the intricate interplay between the position of the chiral center(s) and the ensuing effects of overall molecular conformation on the self-assembly into these fascinating and now even more complex B4 morphologies. As an example of the now realized predictability regarding filament type, dimensions and handedness, let us compare the nanofilaments formed by **A**, **B**, **E**, and **BC5** by using the simplified molecular conformations shown in Figure 10. **BC5** is a de facto mix of the concepts used for **A** (or **B**) and **E** with the average distance of the chiral centers two carbon atoms away from the core-chain juncture. Thus, the observation of FNRs was not a surprise for **BC5**. The bent of the aliphatic side chain in the same direction (see Figure 3b) for **BC5** (3,1 – ^{p}R,^{m}R) mimics the conformation of **B** forming the larger HNF_{mod2bS}, which are observed for **BC5**. Similarly, conformation and configuration of and caused by the chiral center at C-3 for **BC5** lead, as expected, to the formation of filaments with either handedness. Similar predictability arguments related to overall conformation that is clearly affected by chiral center positions and configuration can be made for the other filaments formed by this new series of bent-core molecules.

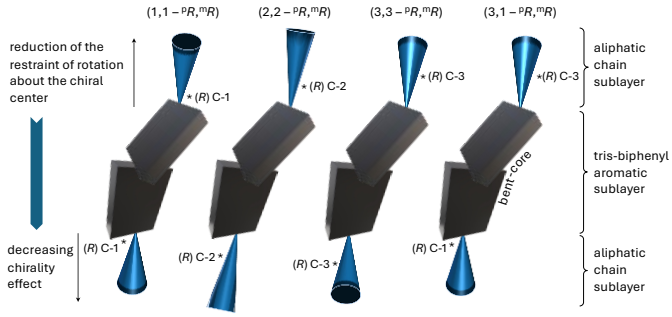

Figure 10. Summary of the interplay between the position(s) of the chiral center(s) and overall conformation of the tris-biphenyl bent-core molecules. Both parameters play key roles in the ensuing formation of the various B4 morphologies. Contributions from both structural effects (configuration of chiral center(s) and overall molecular conformation) can be prota- or antagonistic, variable in the strength of contribution, depending on the position within the molecule (*meta*- vs. *para*-side).

In closing, while further structural modifications with respect to the placement of chiral centers in the aliphatic side chains are certainly possible (and about to be pursued), the set of currently available tris-biphenyl derivatives provides some very powerful insights into the nature of nano- and microfilament formation, and how to best manipulate chemical structures to achieve a specific shape, twist sense, coexistence, and overall filament dimension outcome that can potentially be applied to a range of related systems. B4 nano- and microfilaments are excellent and even dynamic templates for emissive dyes, nanomaterials, and various liquid crystal phases, among other guests,[46-55] and the now more straightforwardly obtainable, ever-increasing number of nano- and microfilament polymorphs will continue to provide geometrically distinct templates for an increasing number of materials and potential applications, and thus access to exciting overall materials properties.[29, 30, 50, 56, 57] For example, alignment of the new, more complex nano- and microfilament types could allow for spatially varying the efficacy of generating circular polarized luminescence (CPL) if nanomaterial or organic molecule emitters are templated by these filaments. Logical blending of nano- and microfilament morphologies (i.e., generating a desired morphology by mixing two others in the melt), as demonstrated by us recently,[58] could further allow the finetuning of such emissive properties that are sought after in encryption technology applications such as physical unclonable functions (PUFs),[59] especially if further coupled with the tunable structural color provided by these nano- and microfilaments.

Author contributions

T.H., M.E.P., and A.G. conceived the idea and the experiments. A.G. with help from G.A. accomplished the syntheses and full analytical characterization of the materials. A.G. performed the POM and CD studies, A.G., G.A., and G.A.A.R. SEM and TEM imaging. M.E.P., S.K.P., and A.S. did the XRD experiments, M.E.P. with some input from T.H. analyzed the XRD data. R.P.L. calculated the conformational energy profiles. G.A.R.R. designed the 3D filament models. T.H. directed the research and wrote the manuscript with contributions from all coauthors.

Conflicts of interest

There are no conflicts to declare.

Data availability

All data needed to evaluate the conclusions discussed in this article are either present in the paper itself or available via the Electronic Supplementary Information (ESI).

Acknowledgements

This work was supported by the National Science Foundation (NSF; DMR-1904091), the Ohio Third Frontier program for Ohio Research Scholars “Research Cluster on Surfaces in Advanced Materials” (T.H.) that supports the Materials Characterization and Imaging Facility at the Advanced Materials and Liquid Crystal Institute (AMLCI) at Kent State University, where current SEM and TEM data were acquired. R.P.L. acknowledges funding from the Natural Sciences and Engineering Research Council of Canada (NSERC). The authors further acknowledge access to the X-ray scattering facility at the AMLCI, which was financially supported by the National Science Foundation (NSF; DMR-2017845), the State of Ohio (The Ohio Department of Higher Education Action Fund), and Kent State University. Finally, we would like to acknowledge the mass spectrometry laboratory at Indiana University for providing all the high-resolution mass spectrometry data.

References

1. A. W. P. Fitzpatrick, B. Falcon, S. He, A. G. Murzin, G. Murshudov, H. J. Garringer, R. A. Crowther, B. Ghetti, M. Goedert and S. H. W. Scheres, *Nature*, 2017, **547**, 185-190.

2. D. Kurouski, X. F. Lu, L. Popova, W. Wan, M. Shanmugasundaram, G. Stubbs, R. K. Dukor, I. K. Lednev and L. A. Nafie, *J. Am. Chem. Soc.*, 2014, **136**, 2302-2312.
3. T. Izoré, D. Kureisaite-Ciziene, S. H. McLaughlin and J. Löwe, *e-Life*, 2016, **5**, e21600.
4. D. M. Bassen, Y. Hou, S. S. Bowser and N. K. Banavali, *Sci. Rep.*, 2016, **6**, 31723.
5. M. A. Constantino, M. Jabbarzadeh, H. C. Fu and R. Bansil, *Sci. Adv.*, 2016, **2**, e1601661.
6. I. Gutsche, A. Desfosses, G. Effantin, W. L. Ling, M. Haupt, R. W. H. Ruigrok, C. Sachse and G. Schoehn, *Science*, 2015, **348**, 704-707.
7. M. C. S. Kingsley and M. A. Ramsay, *Arctic*, 1988, **41**, 236-238.
8. H. L. Kui, X. Y. Liu, J. Liu, W. Liang, S. W. Zhang, Z. H. Qian and L. Ren, *Front. Bioeng. Biotech.*, 2020, **8**, 363.
9. J. S. Wang, G. Wang, X. Q. Feng, T. Kitamura, Y. L. Kang, S. W. Yu and Q. H. Qin, *Sci. Rep.*, 2013, **3**, 3102.
10. A. Gowda, S. K. Pathak, G. A. R. Rohaley, G. Acharjee, A. Oprandi, R. Williams, M. E. Prévot and T. Hegmann, *Mater. Horiz.*, 2024, **11**, 316-340.
11. D. P. N. Gonçalves, M. E. Prévôt, S. Üstünel, T. Ogolla, A. Nemati, S. Shadpour and T. Hegmann, *Liq. Cryst. Rev.*, 2021, **9**, 1-34.
12. L. E. Hough, H. T. Jung, D. Kruerke, M. S. Heberling, M. Nakata, C. D. Jones, D. Chen, D. R. Link, J. Zasadzinski, G. Heppke, J. P. Rabe, W. Stocker, E. Korblova, D. M. Walba, M. A. Glaser and N. A. Clark, *Science*, 2009, **325**, 456-460.
13. R. V. Kohn and E. O'Brien, *J. Elasticity*, 2018, **130**, 115-143.
14. D. Chen, J. E. Maclennan, R. Shao, D. K. Yoon, H. T. Wang, E. Korblova, D. M. Walba, M. A. Glaser and N. A. Clark, *J. Am. Chem. Soc.*, 2011, **133**, 12656-12663.
15. M. M. C. Tortora, G. Mishra, D. Presern and J. P. K. Doye, *Sci. Adv.*, 2020, **6**, eaaw8331.
16. E. Grelet and M. M. C. Tortora, *Nat. Mater.*, 2024, **23**, 1276-1282.
17. G. A. R. Rohaley and T. Hegmann, *Nat. Mater.*, 2024, **23**, 1161-1163.
18. G. Pelzl, S. Diele and W. Weissflog, *Adv. Mater.*, 1999, **11**, 707-724.
19. D. M. Walba, L. Eshdat, E. Korblova and R. K. Shoemaker, *Cryst. Growth Des.*, 2005, **5**, 2091-2099.
20. L. Li, M. Salamonczyk, A. Jákli and T. Hegmann, *Small*, 2016, **12**, 3944-3955.
21. S. Shadpour, A. Nemati, M. Salamonczyk, M. E. Prévôt, J. Liu, N. J. Boyd, M. R. Wilson, C. H. Zhu, E. Hegmann, A. I. Jákli and T. Hegmann, *Small*, 2020, **16**, 1905591.
22. L. Li, M. Salamonczyk, S. Shadpour, C. H. Zhu, A. Jákli and T. Hegmann, *Nat. Commun.*, 2018, **9**, 714.
23. E. Tsai, J. M. Richardson, E. Korblova, M. Nakata, D. Chen, Y. Q. Shen, R. F. Shao, N. A. Clark and D. M. Walba, *Angew. Chem. Int. Ed.*, 2013, **52**, 5254-5257.
24. M. Castillo-Vallés, M. Cano, A. Bermejo-Sanz, N. Gimeno and M. B. Ros, *J. Mater. Chem. C*, 2020, **8**, 1998-2007.
25. M. Alaasar, M. Prehm and C. Tschierske, *Chem.-Eur. J.*, 2016, **22**, 6583-6597.
26. S. Shadpour, A. Nemati, N. J. Boyd, L. Li, M. E. Prévôt, S. L. Wakerlin, J. P. Vanegas, M. Salamonczyk, E. Hegmann, C. H. Zhu, M. R. Wilson, A. I. Jákli and T. Hegmann, *Mater. Horiz.*, 2019, **6**, 959-968.
27. B. Sezgin, J. Liu, D. P. N. Gonçalves, C. H. Zhu, T. Tilki, M. E. Prévôt and T. Hegmann, *ACS Nanosci Au*, 2023, **3**, 295-309.
28. J. Liu, S. Shadpour, M. E. Prévôt, M. Chirgwin, A. Nemati, E. Hegmann, R. P. Lemieux and T. Hegmann, *ACS Nano*, 2021, **15**, 7249-7270.
29. W. Park, T. Ha, T. T. Kim, A. Zep, H. Ahn, T. J. Shin, K. I. Sim, T. S. Jung, J. H. Kim, D. Pociecha, E. Gorecka and D. K. Yoon, *NPG Asia Mater*, 2019, **11**, 45.
30. W. Park, J. M. Wolska, D. Pociecha, E. Gorecka and D. K. Yoon, *Adv. Opt. Mater.*, 2019, **7**, 1901399.
31. J. Y. Sun, B. Bhushan and J. Tong, *RSC Adv.*, 2013, **3**, 14862-14889.
32. J. W. Goodby, A. J. Slaney, C. J. Booth, I. Nishiyama, J. D. Vuijk, P. Styring and K. J. Toyne, *Mol. Cryst. Liq. Cryst.*, 1994, **243**, 231-298.
33. G. Lemahieu, J. Aguilhon, H. Strub, V. Molinier, J. F. Ontiveros and J. M. Aubry, *RSC Adv.*, 2020, **10**, 16377-16389.
34. C. Thiehoff, Y. P. Rey and R. Gilmour, *Isr. J. Chem.*, 2017, **57**, 92-100.
35. A. D. Becke, *J. Chem. Phys.*, 1993, **98**, 1372-1377.
36. R. Ditchfield, W. J. Hehre and J. A. Pople, *J. Chem. Phys.*, 1971, **54**, 724-728.
37. W. J. Hehre and W. A. Lathan, *J. Chem. Phys.*, 1972, **56**, 5255-5257.
38. H. Qi, J. D. O'Neil and T. Hegmann, *J. Mater. Chem.* 2008, **18**, 374-380.
39. C. A. Schneider, W. S. Rasband and K. W. Eliceiri, *Nat. Methods*, 2012, **9**, 671-675.
40. G. M. Grason, *Soft Matter*, 2020, **16**, 1102-1116.
41. D. M. Hall and G. M. Grason, *Interface Focus*, 2017, **7**, 20160140.
42. G. M. Grason, *J. Chem. Phys.*, 2016, **145**, 110901.
43. H. Cui, T. Muraoka, A. G. Cheetham and S. I. Stupp, *Nano Lett.*, 2009, **9**, 945-951.
44. G. W. Gray and D. G. McDonnell, *Mol. Cryst. Liq. Cryst.*, 1976, **34**, 211-217.
45. P. E. S. Silva, J. L. Trigueiros, A. C. Trindade, R. Simoes, R. G. Dias, M. H. Godinho and F. V. de Abreu, *Sci. Rep.*, 2016, **6**, 23413.
46. Y. Cao, T. Y. Tan, D. M. Walba, N. A. Clark, G. Ungar, C. H. Zhu, L. Zhang and F. Liu, *Nano Lett.*, 2022, **22**, 4569-4575.
47. H. Kim, S. H. Ryu, M. Tuchband, T. J. Shin, E. Korblova, D. M. Walba, N. A. Clark and D. K. Yoon, *Sci. Adv.*, 2017, **3**, e1602102.
48. C. H. Zhu, C. Wang, A. Young, F. Liu, I. Gunkel, D. Chen, D. Walba, J. Maclennan, N. Clark and A. Hexemer, *Nano Lett.*, 2015, **15**, 3420-3424.
49. D. Chen, M. R. Tuchband, B. Horanyi, E. Korblova, D. M. Walba, M. A. Glaser, J. E. Maclennan and N. A. Clark, *Nat. Commun.*, 2015, **6**, 7763.
50. R. A. Callahan, D. C. Coffey, D. Chen, N. A. Clark, G. Rumbles and D. M. Walba, *ACS Appl. Mater. Interf.*, 2014, **6**, 4823-4830.
51. D. Chen, C. H. Zhu, H. T. Wang, J. E. Maclennan, M. A. Glaser, E. Korblova, D. M. Walba, J. A. Rego, E. A. Soto-Bustamante and N. A. Clark, *Soft Matter*, 2013, **9**, 462-471.
52. J. Liu, Y. Molard, M. E. Prévôt and T. Hegmann, *ACS Appl. Mater. Interf.*, 2022, **14**, 29398-29411.
53. W. Lewandowski, N. Vaupotic, D. Pociecha, E. Gorecka and L. M. Liz-Marzán, *Adv. Mater.*, 2020, **32**, 1905591
54. M. Baginski, M. Tupikowska, G. Gonzalez-Rubio, M. Wojcik and W. Lewandowski, *Advanced Materials*, 2020, **32**, 1904581.
55. S. Parzyszek, J. Tessarolo, A. Pedrazo-Tardaos, A. M. Ortuño, M. Bagiński, S. Bals, G. H. Clever and W. Lewandowski, *ACS Nano*, 2022, **16**, 18472-18482.
56. H. Kim, Y. Yi, D. Chen, E. Korblova, D. M. Walba, N. A. Clark and D. K. Yoon, *Soft Matter*, 2013, **9**, 2793-2797.
57. G. Park, H. Park, J. M. Wolska, J. G. Park and D. K. Yoon, *Mater. Horiz.*, 2022, **9**, 2542-2550.
58 J. Liu, S. Shadpour, A. Nemati, M. E. Prévôt, E. Hegmann, C. Zhu and T. Hegmann, *Liq. Cryst.*, 2021, **48**, 1129-1139.
59. X. Lin, Q. Li, Y. Tang, Z. Chen, R. Chen, Y. Sun, W. Lin, G. Yi, and Q. Li, *Adv. Sci.*, 2024, **11**, 2401983.

Data availability

All data needed to evaluate the conclusions discussed in this article are either present in the paper itself or available via the Electronic Supplementary Information (ESI).